Revealing the hidden order in $BaTi_2As_2O$ via nuclear magnetic resonance

D. W. Song,[1] J. Li,[1] D. Zhao,[2] L. K. Ma,[1] L. X. Zheng,[1] S. J. Li,[1] L. P. Nie,[1] X. G. Luo,[1,2,3,4] Z. P. Yin,[5,*]
T. Wu,[1,3,4,†] and X. H. Chen[1,2,3,4]

[1]*Hefei National Laboratory for Physical Sciences at the Microscale, University of Science and Technology of China, Hefei, Anhui 230026, China*

[2]*Department of Physics, University of Science and Technology of China, Hefei, Anhui 230026, China*

[3]*Key Laboratory of Strongly-coupled Quantum Matter Physics, University of Science and Technology of China, Chinese Academy of Sciences, Hefei 230026, China*

[4]*Collaborative Innovation Center of Advanced Microstructures, Nanjing 210093, China*

[5]*Department of Physics and Center for Advanced Quantum Studies, Beijing Normal University, Beijing 100875, China*

(Received 11 June 2018; revised manuscript received 6 November 2018; published 20 December 2018)

In low-dimensional metallic systems, lattice distortion is usually coupled to a density-wave-like electronic instability due to Fermi-surface nesting (FSN) and strong electron-phonon coupling [M. D. Johannes and I. I. Mazin, Phys. Rev. B **77**, 165135 (2008)]. However, the ordering of other electronic degrees of freedom can also occur simultaneously with the lattice distortion; thus, it challenges the aforementioned prevailing scenario. Recently, a hidden electronic reconstruction beyond FSN was revealed in a layered metallic compound $BaTi_2As_2O$ below the structural transition temperature $T_s \sim 200$ K. The nature of this hidden electronic instability is under strong debate. Here, by measuring the local orbital polarization through ^{75}As nuclear magnetic resonance experiments, we observe a *p*-*d* bond order between Ti and As atoms in $BaTi_2As_2O$ single crystal. Below T_s, the bond order breaks both rotational and translational symmetry of the lattice. Meanwhile, the spin-lattice relaxation measurement indicates a substantial loss of density of states and an enhanced spin fluctuation in the bond-ordered state. Further, first-principles calculations suggest that the mechanism of the bond order is due to the coupling between lattice and nematic instabilities. Our results strongly support a bond-order-driven electronic reconstruction in $BaTi_2As_2O$ and shed light on the mechanism of superconductivity in this family.

DOI: 10.1103/PhysRevB.98.235142

I. INTRODUCTION

Superconductivity in titanium oxypnictides $BaTi_2Pn_2O$ (Pn = As, Sb, Bi) and their isovalent as well as aliovalent analogies: $BaTi_2(Sb_{1-x}Bi_x)_2O$ and $Ba_{1-x}A_xTi_2Sb_2O$ (A = Na, K, Rb) were recently discovered [1–7]. Because of their quasi-two-dimensional (2D)-layered structures of Ti_2O-plane resembling both cuprates and iron-based superconductors, much attention has been attracted to these materials. In particular, they show a remarkable anomaly in both temperature-dependent charge transport and magnetic susceptibility, which are ascribed to electronic instabilities like charge- or spin-density waves (CDW/SDW) [2,8–11]. Above all, by substitution As in $BaTi_2As_2O$ with the isovalent Sb or Bi, the density-wave transition is gradually suppressed and finally leads to superconductivity. This suggests a similar competition between superconductivity and the density-wave order as in cuprates and iron-based superconductors [2]. Therefore, identifying the exact nature of the possible density-wave order in $BaTi_2As_2O$ is not only crucial for understanding itself, but also of great importance to understand the superconductivity in this family.

To uncover the electronic ordering in titanium oxypnictides $BaTi_2Pn_2O$ (Pn = As, Sb) and $Na_2Ti_2Pn_2O$ (Pn=As, Sb), much effort has been made in previous studies. Early electronic structure calculations predicted that the Fermi surfaces of this family are quite well nested and therefore susceptible to either CDW or SDW instabilities [11–15]. Furthermore, recent calculations on the phonon dispersion also supported lattice instability and Fermi-surface (FSN)-driven CDW in these materials [16,17]. However, most of experiments in this family have failed to give direct evidence for CDW or SDW [18–20]. Instead of superlattice distortion, only a rotational symmetry breaking is observed below the structural transition temperature (T_s) in $BaTi_2As_2O$ [18]. Recently, superlattice distortion has been successfully observed in $Ba_{1-x}Na_xTi_2Sb_2O$ and $Na_2Ti_2Pn_2O$ (Pn = As, Sb), which strongly supports the CDW picture [21,22]. However, in contrast to conventional FSN, the observed partial gap in angle-resolved photoemission spectrum (ARPES) experiment opens on the so-called Fermi patches rather than the Fermi surface, and accompanies an anomalous spectral weight redistribution within a large energy scale [22,24,25]. Theoretically, various local electronic orderings have been proposed beyond charge density-wave picture, including charge/orbital ordering within one unit cell of Ti_2O square [18,26] and spin-driven bond ordering [27]. In these cases, structural transition is driven by electronic instability similar to that in FeSe [28]. To date,

---

[*] yinzhiping@bnu.edu.cn

[†] wutao@ustc.edu.cn

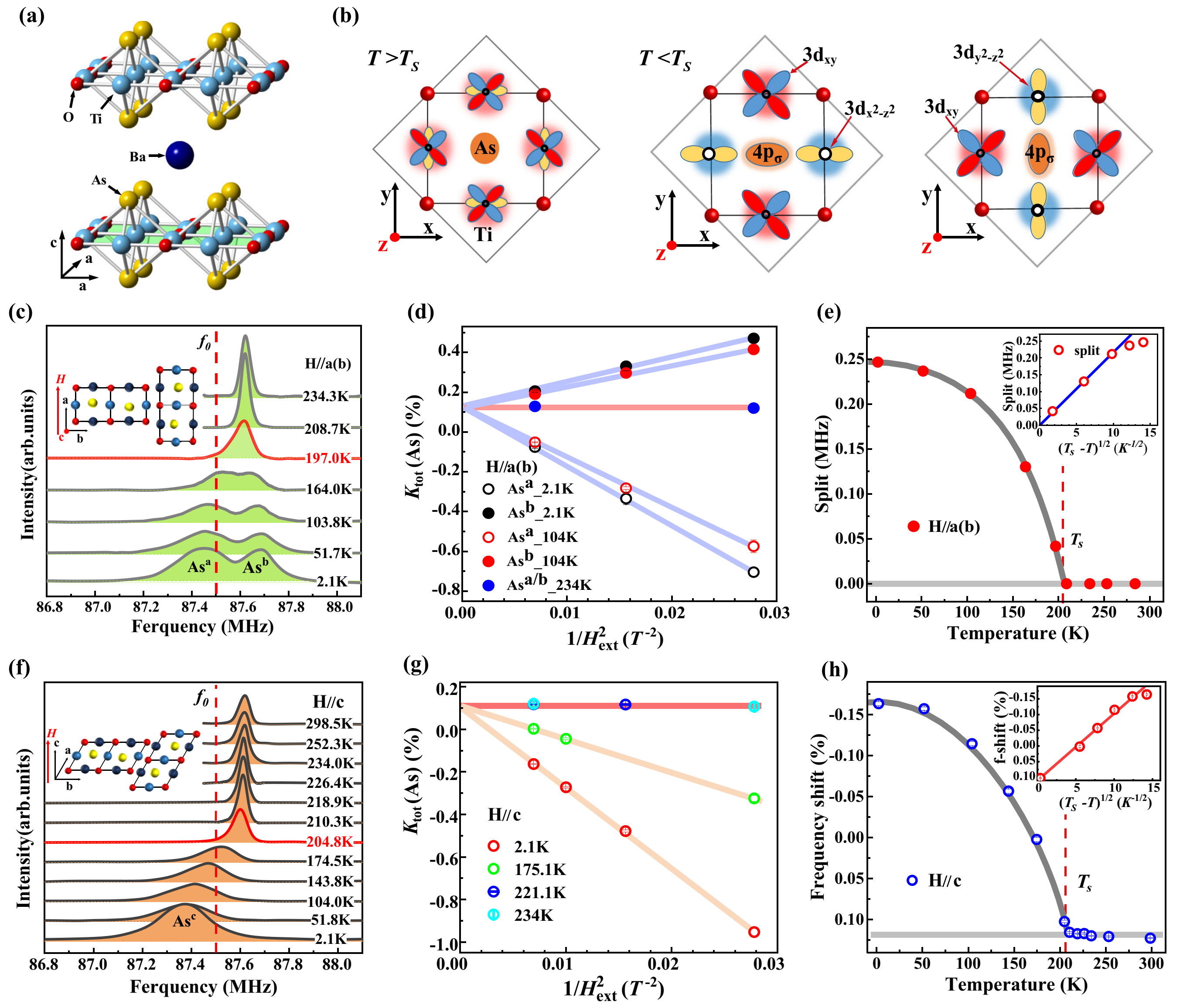

FIG. 1. Evidence for the tetragonal-to-orthorhombic structural transition and $4p_\sigma$ orbital polarization in $BaTi_2As_2O$. (a) Crystallographic structure of $BaTi_2As_2O$ with $[Ti_2As_2O]^{2-}$ and Ba^{2+} layers stacked alternatively along c axis. (b) Possible configuration of orbital polarization in each structural domain above and below structural transition temperature T_s. Below T_s, the polarized $4p_\sigma$ orbital of As with the $3d$ orbital order of Ti [18,26] breaks the rotational symmetry. (c), (f) Temperature-dependent ^{75}As NMR central transition lines measured at $H_{\text{ext}} \parallel [100]$ ($H_{\text{ext}} \parallel a/b$) and $H_{\text{ext}} \parallel [001]$ ($H_{\text{ext}} \parallel c$). Below T_s, there is a substantial quadrupole contribution on the central transition line. (d), (g) The field-dependent total Knight shift ($K_{\text{tot}} = \frac{\nu}{\gamma_n H_{\text{ext}}} - 1$) of As^a/As^b and As^c at different temperatures. The bold lines are guides for the eye. (e) The temperature-dependent splitting of NMR central line with $H_{\text{ext}} \parallel a(b)$ and (h) the negative frequency-shift of NMR central line with $H_{\text{ext}} \parallel c$. Both of them can be taken as order parameters, showing typical $\sqrt{T_s - T}$ behavior of a second-order phase transition (see the inset).

direct experimental confirmation for the electronic order is still missing in this family. Especially, how to verify the possible ordering phenomenon in orbital degrees of freedom is challenging.

Here, we use nuclear magnetic resonance (NMR) technique to investigate the local orbital polarization at As sites in $BaTi_2As_2O$ single crystals. In one unit cell, as shown in Fig. 1(b), one As atom and four nearest-neighboring Ti atoms are connected by *p-d* covalent bonds. The orbital polarization at both As and Ti sites is strongly dependent on the status of the *p-d* covalent-bond. In the high-temperature tetragonal phase, since the four *p-d* covalent bonds between Ti and As atoms are equivalent, there is no in-plane polarization on As $4p_\sigma$ orbitals. However, below structural transition temperature T_s, we found that the orbital polarization of As $4p_\sigma$ orbitals shows a remarkable change beyond naive orthorhombic structural distortion [18], indicating a significant modulation of the *p-d* covalent-bond stat, which is defined as bond order (BO) [32]. This is the main finding in the present paper.

II. METHODS

A. Sample growth

High-quality BaTi$_2$As$_2$O single crystals were grown by a BaAs self-flux method. The flux BaAs was prepared by reacting Ba and As in a sealed quartz tube and heated at 800 °C for 12 h. This precursor was then mixed with BaO, Ti and As powders at the ratio of BaO: Ti: As: BaAs = 1:2:2:2.8. The mixture was loaded into an alumina crucible and sealed in a pure titanium crucible, and then placed in a tube furnace, quickly heated to 800 °C at the atmosphere of Argon and kept for 12 h. The tube furnace was then heated up to 1200 °C at the rate of 40 °C/h and kept for 24 h. Before turning off the power, the tube furnace was then slowly cooled down to 900 °C at a rate less than 3 °C/h.

B. NMR technique

The standard NMR spin-echo techniques were used with a commercial NMR spectrometer from Thamway Co. Ltd. The external magnetic field was generated by a 16-tesla magnet from Oxford Instruments. The ^{75}As NMR spectra of BaTi$_2$As$_2$O single crystal were obtained by sweeping the frequency at fixed magnetic field and then gluing the Fourier transform of spin-echo signal for all measurements. For NMR technique, when the nuclear spin number (I_s) is equal to 1/2, the Knight shift extracted from the NMR central transition line mainly comes from the magnetic hyperfine interaction between nuclear and electrons, which is related to local spin susceptibility (χ_s), such as ^{77}Se ($I_s = 1/2$) in FeSe [29,30]. However, when I_s is larger than 1/2, the Knight shift extracted from the NMR central transition line also has an additional contribution from the second-order effect of the nuclear quadrupole interaction (NQI). When taking the NQI as a perturbation, the calculated NMR frequency of the central transition line to the second order for ^{75}As ($I_s = 3/2$) is expressed as [31]

$$\begin{aligned}\nu = {} & \gamma_{\rm n} H_{\rm ext}(\mathbf{K}{+}1) + \frac{{\nu_{\rm Q}}^2}{\gamma_{\rm n} H_{\rm ext}(\mathbf{K}{+}1)} \left\{ \frac{\sin^2\theta}{16} \left[3\left(1 - \frac{2}{3}\eta\cos 2\phi\right) \right.\right. \\ & \left.\left. - \; 27\cos^2\theta \left(1 + \frac{2}{3}\eta\cos 2\phi\right)\right)\right] + \frac{\eta^2}{96}[24\cos^2\theta \\ & \left. + \, 17\cos^2 2\phi \sin^4\theta - 16] \right\} \\ = {} & \gamma_{\rm n} H_{\rm ext}(\mathbf{K}+1) + \frac{f(\nu_{\rm Q}, \eta, \theta, \phi)}{\gamma_{\rm n} H_{\rm ext}(\mathbf{K}+1)}, \qquad (1)\end{aligned}$$

where $\mathbf{K}$ is the Knight shift tensor due to the magnetic hyperfine interaction obtained by

$$\mathbf{K} = K_x \sin^2\theta\cos^2\phi + K_y \sin^2\theta \sin^2\phi + K_z\cos^2\theta, \qquad (2)$$

θ as well as ϕ are the polar angles of the applied magnetic field ($H_{\rm ext}$) with respect to the principal axis frame, which is the same with the lattice coordinate system in the tetragonal phase. $\gamma_{\rm n}$ is the nuclear gyromagnetic ratio (for ^{75}As, $\gamma_{\rm n} = 7.2919$ MHz/T) and $H_{\rm ext}$ is the applied magnetic field. The asymmetry parameter η is defined as $\eta = |\frac{V_{\rm xx}-V_{\rm yy}}{V_{\rm zz}}|$, where $|V_{\rm xx}| \leqslant |V_{\rm yy}| \leqslant |V_{\rm zz}|$ are the principal components of the electric field gradient (EFG) at ^{75}As site. $\nu_{\rm Q}$ is the quadrupole frequency, defined as $\nu_{\rm Q} = \frac{eQV_{zz}}{\hbar}$, where e is the elementary electric charge and Q is the electric quadrupole moment of ^{75}As nuclei. According to Eq. (1), the total Knight shift is expressed as

$$\mathbf{K}_{\rm tot} = \frac{\nu}{\gamma_{\rm n} H_{\rm ext}} - 1 = \mathbf{K} + \frac{f(\nu_{\rm Q}, \eta, \theta, \phi)}{(\gamma_{\rm n} H_{\rm ext})^2(\mathbf{K}+1)}, \qquad (3)$$

where the second term is the NQI contribution proportional to $1/H_{\rm ext}^2$. In this work, through a comprehensive study on the quadrupole contribution to the ^{75}As NMR central spectra, we successfully obtained the information on orbital polarization of As $4p_\sigma$ orbital, which revealed a BO between As and Ti below the structural transition temperature T_s.

C. Theoretical calculation

The electronic structure and spin dynamics were computed using density-functional theory combined with dynamical mean-field theory (DFT+DMFT) [40], where the DFT part is based on the linearized augmented plane-wave method as implemented in WIEN2k [41]. Instead of constructing correlated orbital from Wannier functions, we used the projection and imbedding process as detailed in Ref. [42]. The impurity problem in DFT+DMFT calculations was solved using continuous-time quantum Monte Carlo method [43,44], with Hubbard $U = 5.0$ eV and Hund's coupling $J = 0.8$ eV at temperature $T = 116$ K. The spin dynamic was computed using the method detailed in Ref. [45]. The phonon dispersion and electron-phonon coupling were computed using the density-functional perturbation theory as implemented in the Quantum ESPRESSO package [46,47], together with the Perdew-Burke-Ernzerhof exchange-correlation functional [48]. We use 80 (800) Ry kinetic energy cutoff for wave functions (charge density and potential), 16 × 16 × 8 k mesh, and 8 × 8 × 4 q mesh, whereas a finer 32 × 32 × 16 k mesh was used to sample the Fermi surface for computing the electron-phonon coupling. The experimentally determined crystal structures including the internal atomic positions were used in all calculations [8].

III. EXPERIMENTAL RESULTS

A. Temperature- and field-dependent ^{75}As NMR central transition lines: Evidence for remarkable $4p_\sigma$ orbital polarization below T_s

Figures 1(c) and 1(f) are the temperature-dependent ^{75}As NMR central transition lines measured in BaTi$_2$As$_2$O single crystal under two different configurations with $H_{\rm ext} \parallel [100]$ [Fig. 1(c)] and $H_{\rm ext} \parallel [001]$ [Fig. 1(f)]. Above T_s, the central transition lines are narrow and symmetric for both configurations with a linewidth of about 40 kHz. As temperature drops below T_s, the central transition line with $H_{\rm ext} \parallel [100]$ splits into two lines, assigned as As^a ($H_{\rm ext} \parallel a$) and As^b ($H_{\rm ext} \parallel b$). Such splitting is ascribed to the tetragonal-to-orthorhombic structural transition at T_s, because the twinning of the orthorhombic domains makes each domain point either along the direction of $H_{\rm ext}$ or orthogonal to $H_{\rm ext}$, as sketched in Fig. 1(c). If we take the splitting as an order parameter, see Fig. 1(e), the temperature-dependent splitting is proportional to $\sqrt{T_s - T}$, which is consistent with a second-order phase transition in Landau theory. Furthermore, the structural orthorhombicity revealed by previous neutron diffraction is perfectly scaled with the observed NMR line splitting, suggesting that both of them are related to the same Landau order parameter (see Fig. 7 in Appendix B). When $H_{\text{ext}} \parallel [001]$ or [110], all orthorhombic domains are equivalent; hence, we only observe a single central transition line in these cases below T_s (see Figs. 1(f) and 6 in Appendix A).

A similar phenomenon is also observed for the tetragonal-to-orthorhombic structural transition in ^{75}As NMR study of LaFeAsO [33], in which the splitting of the central transition line is dominated by the second order effects of the NQI. According to Eq. (1), the magnetic contribution on NMR frequency is proportional to H_{ext}, while the quadrupole contribution on NMR frequency should be proportional to $\frac{1}{H_{\text{ext}}}$. As shown in Fig. 1(d), the field-dependent total Knight shift ($K_{\text{tot}} = \frac{\nu}{\gamma_n H_{\text{ext}}} - 1$) confirms that the splitting of the central transition line with $H_{\text{ext}} \parallel [100]$ is also dominated by the second-order effects of the NQI. The extrapolated magnetic Knight shift at $H_{\text{ext}} \rightarrow \infty$ only has a tiny contribution on the total splitting of the central transition line (see Fig. S4 in Supplemental Material [49]) and is not our focus in the present paper. Furthermore, although there is no splitting in the central transition line with $H_{\text{ext}} \parallel [001]$, a significant negative frequency shift appears below T_s, which is also due to the second-order effects of NQI [Fig. 1(g)]. As shown in Fig. 1(h), such negative frequency shift follows the same temperature dependence as that of the splitting with $H_{\text{ext}} \parallel [100]$. Usually, when the magnetic field is applied along the principal axis of the EFG tensor, the quadrupole contribution on the NMR frequency of the central transition line disappears unless asymmetry parameter η is nonzero. In a previous NQR study, $\eta \neq 0$ due to the tetragonal-to-orthorhombic structural transition has already been observed below T_s on BaTi$_2$Sb$_2$O [19]. However, the negative slopes for both As^a and As^c in Figs. 1(d) and 1(g) suggest that, besides $\eta \neq 0$, the principal axis of the EFG tensor must be rotated away from [001] direction, which is the principal axis of the EFG tensor in the tetragonal phase. All these results suggest that there is a remarkable change in EFG tensor after structural transition at T_s.

In principle, the origin of EFG tensor can be divided into two parts [34]: one comes from the neighboring ions as point charges, which is defined as lattice contribution; the other is from the on-site electrons of partially filled orbital, which is defined as valence contribution. Based on the point-charge model, we have studied the lattice contribution to the total EFG tensor (see Fig. 9 in Appendix D). We found that both of the tetragonal-to-orthorhombic structural transition and the possible charge order at Ti sites [18] have negligible effect on the EFG tensor through lattice contribution. Therefore, the remarkable change in the EFG tensor below T_s (ν_Q increased about one order of magnitude, see the next section for details) should be ascribed to the valence contribution at ^{75}As sites. As mentioned above, the valence contribution is related to the partially filled orbital. When the orbitals are spherically symmetric or nonpolarized in total, the valence contribution on EFG tensor is zero. To explain the significant enhancement of EFG tensor due to valence contribution below T_s, a strong polarization of the partially filled orbital is needed. Considering the $4p_\sigma$ ($\sigma = x, y, z$) orbital as the partially filled orbital at ^{75}As sites, our results strongly support the significant orbital polarization for $4p_\sigma$ orbital at ^{75}As sites below T_s, which is probably due to the *p-d* bond ordering between Ti and As atoms. In the next section, through a comprehensive study on the angular dependent NMR spectra, the *p-d* bond ordering between Ti and As atoms is further confirmed.

B. Angular-dependent ^{75}As NMR central transition lines: Evidence for *p-d* bond order

As shown in Fig. 2, we further performed an angular dependent measurement on ^{75}As NMR central transition lines at 245.5 K [tetragonal phase, Fig. 2(a)] and 2.1 K [orthorhombic phase, Fig. 2(c)], respectively. In the tetragonal phase, the angular-dependent central transition line shows a very tiny angular dependence, which can be fitted well by Eq. (1) [see Fig. 2(b)] and gives $\nu_Q \approx 0.57$ MHz, $\eta = 0$, and $d\theta = 0$. Here, $d\theta$ is the angle between the principal axis of the EFG tensor and the crystallographic *c* axis. Based on the discussions on the EFG tensor above, the small value of ν_Q suggests a possible weak polarization of $4p_\sigma$ orbital above T_s. However, below T_s, the central transition lines for both As^a and As^b show a strong angular dependence and are highly symmetrical with respect to $\theta = 0$ ($H_{\text{ext}} \parallel c$), see Fig. 2(c). The angular dependent central frequency of As^a (red dots) and As^b (green dots) are shown in Fig. 2(d). For domain As^a, the two symmetrical maximums located at $\theta \approx 49°$ and $\theta \approx -49°$ are corresponding to two mirror symmetric principal axes of the EFG tensor [31] with respect to $\theta = 0$, indicative of two different ^{75}As sites in each domain, assigned as As(1) and As(2) (see the Supplemental Material). This suggests that both the fourfold rotational symmetry and translational symmetry are breaking below T_s. Since the angle between these two principal axes is close to 90°, the central frequency of As(1) and As(2) exhibit a very similar angular dependence. Combined with the realistic broadening effect, the central lines of As(1) and As(2) are always overlapped and can hardly be distinguished from the total spectra. More supporting evidence for two nonequivalent ^{75}As sites is the symmetrical linewidth with respect to $\theta = 0$, which is not consistent with only one ^{75}As site (see the Supplemental Material). For domain As^b, since the principal axis of the EFG tensor for As(1) and As(2) are mirror symmetrical with respect to the field-rotational plane, the angle between H_{ext} and these two principal axes are exactly equal and always larger than the value of approximately 49°. To quantitatively analyze the angular-dependent measurements, the NMR central frequency for both As^a and As^b are well fitted [Fig. 2(d)] by the modified Eq. (1) as follows:

$$\nu = \gamma_n H(K+1) + \frac{f(\nu_Q, \eta, \theta, d\theta, \phi) + f(\nu_Q, \eta, \theta, -d\theta, \phi)}{\gamma_n H(K+1)}, \tag{4}$$

where the second term is the average of the quadrupole contribution from As(1) and As(2). On the basis of considering an azimuthal-angle transformation (see the Supplemental Material) for domain As^b, the angular-dependent central frequency for domain As^a and As^b [Fig. 2(d)] can be perfect simultaneously fitted by Eq. (4) and gives a set of identical

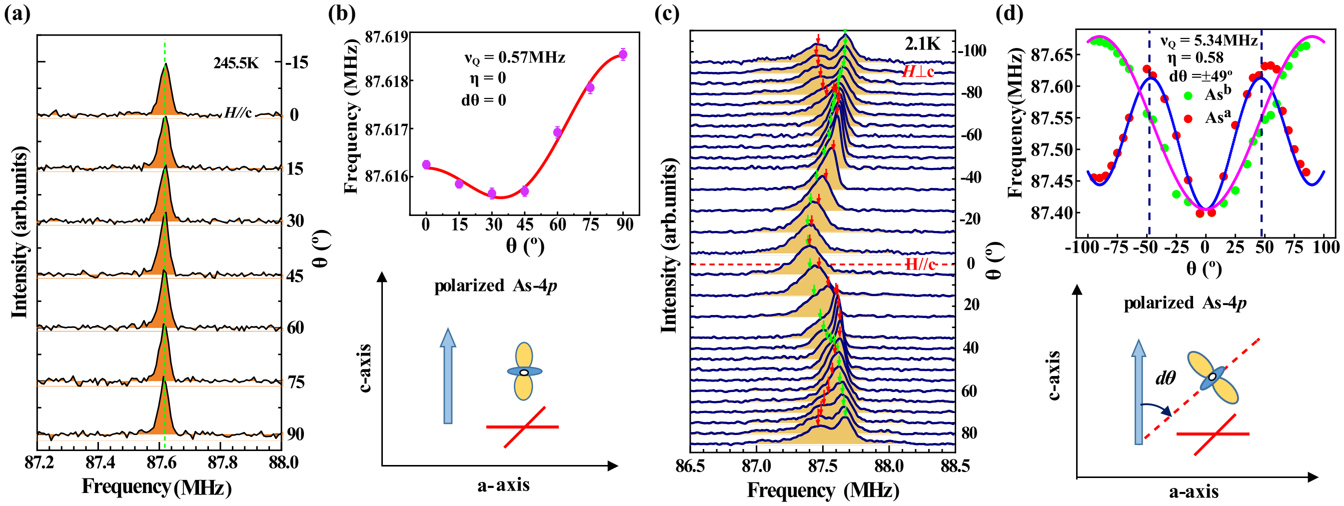

FIG. 2. Determination of angular-selective polarization for $4p_\sigma$ orbital below T_s. (a), (c) Azimuthal-angle dependence of ^{75}As NMR central lines at tetragonal and orthorhombic phases, respectively. θ is defined as the angle between the applied magnetic field $H_{\rm ext}$ and the crystallographic c axis, where $\theta = 0$ is corresponding to $H_{\rm ext} \parallel c$. The red and green arrows in (c) are guides to the eye to show the evolution of the NMR central frequency for domain As^a and As^b with θ. (b) and (d) show the angular dependence of the NMR central frequency extracted from (a) and (c), respectively. The colorful solid lines (pink and blue) are the fitting results by using Eq. (4) with a set of identical parameters.

parameters with $\nu_Q \approx 5.34$ MHz, $d\theta = 49^\circ$, and $\eta = 0.58$. Compared to the tetragonal phase, ν_Q increases by about one order of magnitude from 0.57 MHz to 5.34 MHz, supporting a significant change of the EFG tensor at ^{75}As sites. As discussed above, such a drastic change on the EFG tensor is due to the polarization of $4p_\sigma$ orbital at ^{75}As sites, suggesting an enhanced covalent bond between Ti and As atoms. Additional important information from the angular-dependent measurements is $d\theta \approx 49^\circ$, which is almost the same as the angle of 48.74° between Ti-As bond direction and the c axis. This unambiguously proves that the principal axis of the EFG tensor is rotated from c axis to one of the Ti-As bond direction, suggesting a specific Ti-As BO.

Next, we would like to use the above NMR results to constrain the BO arrangement in real space. First, the specific orbital polarization of As $4p_\sigma$ orbital due to BO needs As atoms to shift from the central axis of the Ti_2O square toward one of the Ti sites [assigned as Ti(y)]. Such local structural distortion breaks the rotational symmetry, coinciding with the tetragonal-to-orthorhombic structural transition in this system. On the other hand, the BO also needs to lower the energy level of $3d_{x^2-z^2}$ on Ti(y) to strengthen the orbital hybridization for the selective Ti-As bond. Therefore, the local structural distortion and orbital polarization are highly correlated through BO, which is indicated by the consistent temperature-dependent behavior between the orbital polarization by NMR and the orthorhombic distortion by neutron diffraction [18]. Second, since there are two different ^{75}As sites in each orthorhombic domain as proved above, the long-ranged BO should also break the translational symmetry of the lattice. This is beyond the previous neutron scattering result [18]. Such translational symmetry breaking is also confirmed by very recent Raman and resonant x-ray scattering experiments [35], which also supports the existence of two different As sites in each orthorhombic domain. Here, based on the previous theoretical calculation [16], we consider two kinds of translational symmetry breaking with a $1 \times 2 \times 1$ superlattice or a $2 \times 2 \times 1$ superlattice, respectively. As shown in Fig. 3, we proposed two possible types of BO model (Model A and

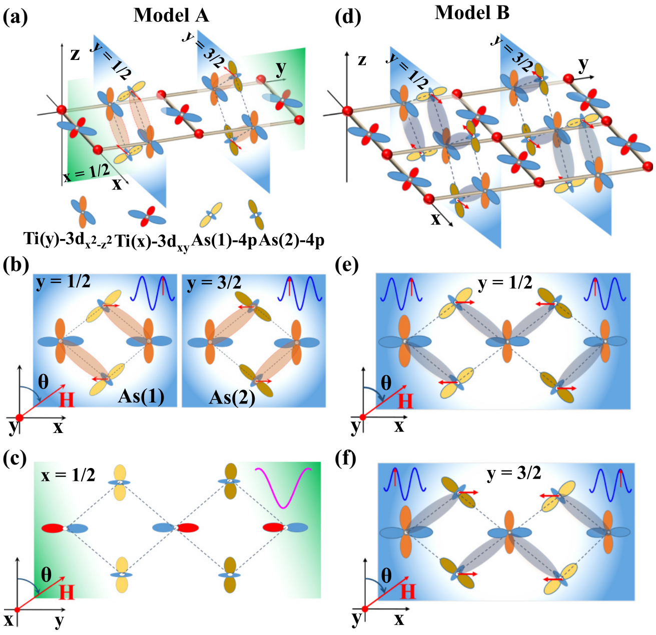

FIG. 3. Schematic models of possible p-d bond order between Ti and As atoms in $BaTi_2As_2O$. (a), (d) The two types of Ti-As bond orders within a $1 \times 2 \times 1$ (Model A) and a $2 \times 2 \times 1$ (Model B) superlattice unit cell combined with the possible orbital order on Ti sites. Planes (b), (c) and (e), (f) are the projections of Model A and Model B on the rotational plane of **H**, where (b), (e), and (f) are corresponding to domain As^a, (c) is corresponding to domain As^b. Red arrows on As mark the relative displacement of As atoms below T_S, the insert solid curves illustrate the corresponding behavior of the central peaks.

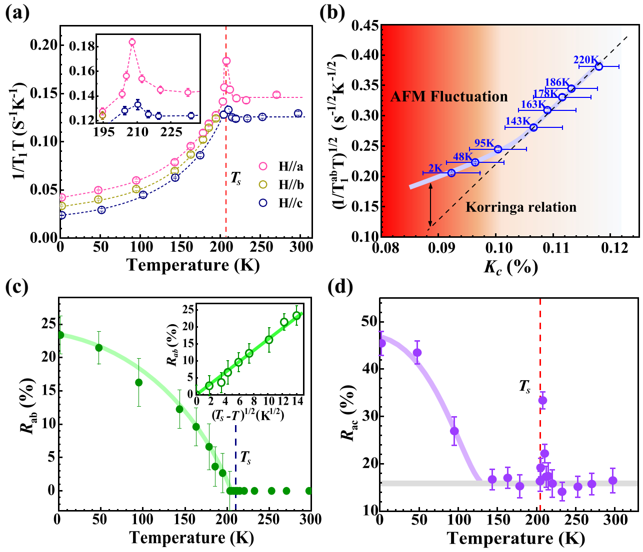

FIG. 4. Evidence for gap opening and enhanced spin fluctuation in bond-ordered state. (a) The temperature-dependent $(T_1T)^{-1}$ for $H_{\text{ext}} \parallel c$ and $H_{\text{ext}} \parallel ab$. (b) $(1/(T_1T))^{-1/2}$ with $H_{\text{ext}} \parallel ab$ vs K_c plot. The dashed line shows the Korringa relation. The deviation from the Korringa relation is clearly observed below 100 K. Moreover, the upturn behavior is consistent with an enhanced antiferromagnetic (AF) fluctuation as similar as that in FeSe [30]. (c) The defined out-of-plane anisotropy R_{ac} and (d) the in-plane anisotropy R_{ab} of spin-lattice relaxation rate deduced from the data in (a). The out-of-plane anisotropy ratio is defined as: $R_{ac} = 2 \times \frac{\frac{1}{2}\times[(T_1T)_a^{-1}+(T_1T)_b^{-1}]-(T_1T)_c^{-1}}{\frac{1}{2}\times[(T_1T)_a^{-1}+(T_1T)_b^{-1}]+(T_1T)_c^{-1}} \times 100\%$ and the in-plane anisotropy ratio is defined as: $R_{ab} = 2 \times \frac{(T_1T)_a^{-1}-(T_1T)_b^{-1}}{(T_1T)_a^{-1}+(T_1T)_b^{-1}} \times 100\%$. The inset in (c) shows typical $\sqrt{T_s - T}$ behavior of a second-order Landau phase transition. The sharp peak around T_S in (d) indicates that the critical spin fluctuation is also *ab*-plane polarized AF fluctuation as that below 100 K.

Model B) with both rotational and translational symmetries breaking. In Model A, the strongest or selective bonding between Ti and As atom is between Ti(y) sites and the nearest two As(1) or two As(2) sites, which exhibits a "\" shape arrangement in real space, while in Model B the strongest or selective bonding between Ti and As atom is between Ti(y) sites and the nearest As(1) and As(2) sites, which exhibits a "∨" shape arrangement in real space. Based on Model A or B, the physical explanation for the angular-dependent central frequency for domain As^a and As^b can be explicitly understood as shown in Figs. 3(b), 3(c), 3(e), and 3(f). Therefore, the present NMR results definitely prove a *p-d* BO between Ti and As atoms in BaTi$_2$As$_2$O below the structural transition temperature, which breaks both rotational and translational symmetries of the lattice. Next, we will further investigate the change of low-energy dynamic spin susceptibility in the bond-ordered state.

C. Temperature-dependent spin-lattice relaxation rate: Evidence for gap opening and enhanced spin fluctuation

Figure 4(a) shows the temperature-dependent spin-lattice relaxation rate divided by temperature, $1/(T_1T)$. Above T_s, $1/(T_1T)$ shows a very weak temperature dependence. Upon cooling, a sharp peak due to critical fluctuation shows up around T_s. Below T_s, $1/(T_1T)$ drops quickly and finally becomes saturated at low temperature. In general, the total relaxation rate could be divided as $1/(T_1T) = 1/(T_1T)_{\text{FL}} + 1/(T_1T)_{\text{SF}}$. $1/(T_1T)_{\text{FL}}$ is the contribution from a Fermi liquid and $1/(T_1T)_{\text{SF}}$ is due to additional spin fluctuations. For a Fermi liquid, $1/(T_1T)_{\text{FL}} \propto K_s^2 \propto N^2(E_F)$, which is called the Korringa relation. As shown in Fig. 4(b), the Korringa relation is satisfied above ∼100 K. This suggests that the initial decrease of $1/(T_1T)$ below T_s is due to the suppression of density of states (DOS) at Fermi level, which is consistent with a partial energy gap in the previous ARPES experiment [24]. Below ∼100 K, the $(1/T_1^{ab}T)^{1/2}$ vs K_c plot clearly deviates from the Korringa relation, suggesting the rising of antiferromagnetic (AF) fluctuations.

To further clarify the AF fluctuations, we plot the temperature-dependent anisotropy of $1/(T_1T)$. As shown in Figs. 4(c) and 4(d), the temperature dependencies for R_{ac} and R_{ab} are quite different. Below T_s, the value of R_{ab} is immediately increased and shows a similar $\sqrt{T_s - T}$ behavior as that of the NMR splitting, which is ascribed to the change of hyperfine coupling tensor due to the BO. However, the value of R_{ac} only changes below ∼100 K instead of T_s, which cannot be explained by the change of hyperfine coupling tensor alone. According to the symmetry analysis of the hyperfine coupling tensor and the remarkable anisotropic critical spin fluctuation around T_s, the enhancement of the R_{ac} below ∼100 K is ascribed to *ab*-plane polarized AF fluctuations with a possible Q_{AF} centered at (π, π) (see the Appendix for details), which suggests enhanced AF fluctuations at low temperature. Theoretically, spin-driven nematic orbital/BO has already been proposed for the BaTi$_2$Pn$_2$O (Pn = As, Sb) family [26,27], which should boost the spin fluctuations below nematic transition temperature as similar as that in an Fe-based superconductor [29,30,33]. Therefore, our spin-lattice relaxation result suggests an important role of the spin-driven nematic instability on BO in BaTi$_2$As$_2$O.

IV. DISCUSSION

To further understand the relevant physics of BO, we carry out first-principle calculations on BaTi$_2$As$_2$O with tetragonal crystal structure. As shown in Fig. 5(d), the lattice dynamics calculation indicates a negative (imaginary) frequency around *X* and *R* points due to strong electron-phonon coupling, suggesting a lattice instability with translational symmetry breaking. This is consistent with previous phonon dispersion calculations and supports a lattice-distortion-induced CDW picture [16]. In the conventional CDW picture, the energy gap opens at the nested section of the Fermi surface, see Fig. 5(b), leading to a metal-insulator phase transition when all Fermi surfaces are gapped, such as transition metal dichalcogenides (TMDs) [36]. However, the electronic reconstruction as revealed by ARPES cannot be explained well by the FSN, but is in favor of a peculiar spectra weight redistribution [22,24,25]. Here, based on our present NMR findings, we proposed that the electronic reconstruction below T$_s$ is mainly affected by the Ti-As BO instead of CDW order. This is somehow consistent with an orbital-order scenario proposed by Nakaoka *et al.*

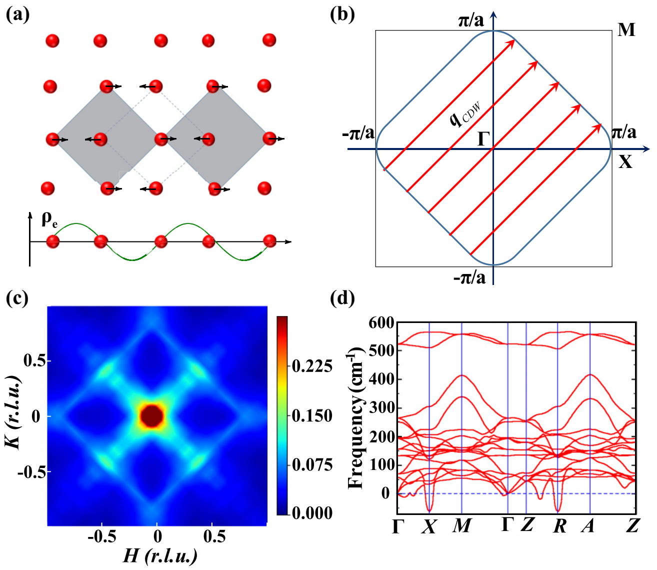

FIG. 5. Conventional CDW picture and theoretical investigation on the lattice and nematic instabilities of $BaTi_2As_2O$. Schematic of traditional CDW in a quasi-2D structure accompanied with (a) supperlattice distortion and (b) Fermi surface nesting. (c) The calculated 2D momentum-dependent spin excitations at $\omega = 5$ meV. (d) The calculated phonon dispersions of $BaTi_2As_2O$. Here, all the calculations were performed using tetragonal $P4/mmm$ symmetry.

[26], in which orbital order is driven by spin fluctuation due to Aslamazov-Larkin vertex correction mechanism. In Fig. 5(c), the calculated low-energy spin excitation spectrum in the tetragonal phase indicates that, besides a primary spin excitation around $Q = (0, 0)$, there is also a substantial contribution from $Q \neq (0, 0)$ even without structural distortion. This result suggests a possible spin-driven nematic fluctuation even without lattice instability. Therefore, although the phonon-induced lattice instability could lead to a conventional CDW order, the nematic instability might overwhelm the CDW instability and dominate the electronic reconstruction below the structural transition temperature. This might be the reason why the BO instead of CDW order becomes the leading electronic order in this system. At the present stage, while it is difficult to disentangle the explicit role of lattice and nematic instabilities on the BO, the BO should be a consequence of the interplay of lattice and nematic instabilities.

Recently, a Hebel-Slichter coherent peak in $1/(T_1T)$ has been observed in $BaTi_2Sb_2O$ by NQR experiment [19], which supports a electron-phonon mediated Bardeen-Cooper-Schrieffer (BCS) superconductivity. Previous calculations indicated that the superconducting transition temperature T_c due to electron-phonon coupling (~2 K) is very close to the experimental value of ~1 K in $BaTi_2Sb_2O$ [16]. Similar calculations also suggested phonon-mediated superconductivity with T_c about 8 K in $BaTi_2As_2O$ with $1 \times 2 \times 1$ superlattice, which is however not observed in experiments [16]. Based on the present findings, one possible explanation is that the BO might be a competing order against superconductivity. When the BO is robust in $BaTi_2As_2O$ with higher T_s, the expected BCS superconductivity is strongly suppressed. This is quite similar to the relationship between nematic order and superconductivity in Fe-based superconductors [28]. Further study on quantum melting of the BO and its relationship with superconductivity could be a key to decode the mechanism of superconductivity in this family. On the other hand, the similar electronic reconstruction observed in $BaTi_2As_2O$ has also been widely observed in many TMDs [37,38], which are ascribed to CDW order with strong electron-phonon coupling [39]. Our present findings suggest that a possible orbital-relevant ordering could also emerge in these materials. This is consistent with some recent study on orbital order in 1T-TaS_2 [50,51]. It will be very interesting to revisit these CDW materials by searching orbital/BO, which will promote the understanding of the underlying physics in TMDs.

V. CONCLUSION

In summary, we successfully revealed a hidden BO below structural transition temperature in $BaTi_2As_2O$ single crystal by studying the second-order quadrupole effect on the NMR central transition line of ^{75}As nuclei. Our results indicate that, besides the rotational symmetry broken observed by previous neutron scattering experiments, the pattern of BO in real space also breaks translational symmetry below T_s. In addition, the spin-lattice relaxation measurement indicates a substantial loss of DOS and an enhanced spin fluctuation in the bond-ordered state. Combining the first-principles calculations on spin excitations, we further discussed the mechanism of the BO in terms of the coupling between lattice and spin-driven nematic instabilities. Finally, we also offer some possible implications of BO on electronic reconstruction and superconductivity in this system.

ACKNOWLEDGMENTS

The authors are grateful for the stimulating discussions with Prof. Y. Li, Prof. Y. Liu, and the help of the Laue diffraction experiment from Dr. Y. J. Yan and Prof. D. L. Feng. This work is supported by the National Key R&D Program of the MOST of China (Grants No. 2016YFA0300201, No. 2017YFA0303000, and No. 2016YFA0302300), the National Natural Science Foundation of China (Grants No. 11522434, No. U1532145, and No. 11674030), the Fundamental Research Funds for the Central Universities and the Chinese Academy of Sciences. The calculations used high-performance computing clusters of Beijing Normal University in Zhuhai and the National Supercomputer Center in Guangzhou. T.W. and Z.P.Y. acknowledge the Recruitment Program of Global Experts. T.W. acknowledges the Chinese Academy of Sciences Hundred Talent Program.

APPENDIX A: DIRECT EVIDENCE FOR C_4 SYMMETRY BREAKING

In the main text, we have figured out that the splitting of the NMR central transition line with $H_{ext} \parallel [100]$ is due to the twinning structure caused by the in-plane C_4 symmetry breaking below T_s. As shown in the upper panel of Fig. 6, in contrast to the splitting of NMR central transition line with $H_{ext} \parallel [100]$, a single NMR central transition line is observed

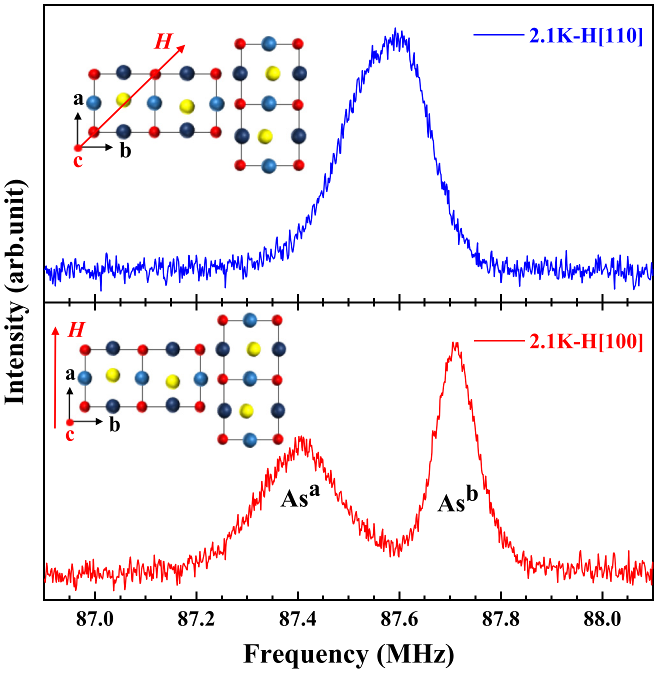

FIG. 6. ^{75}As NMR central transition lines for the BaTi$_2$As$_2$O single crystal with magnetic field $H_{\text{ext}} \parallel [110]$ (upper panel) and $H_{\text{ext}} \parallel [100]$ (lower panel) at 2.1 K, respectively. Insert: schematic of the twinning structures.

with $H_{\text{ext}} \parallel [110]$. This is also consistent with the in-plane C_4 symmetry breaking below T_s.

APPENDIX B: THE SCALING OF ORDER PARAMETERS BETWEEN BOND ORDER AND STRUCTURAL DISTORTION

As shown in Fig. 7, the splitting, which has been proved as an order parameter for the Ti-As bond ordering, can be perfectly scaled with the orthorhombicity α measured by neutron diffraction [18], suggesting that both of them are related to the same Landau-type order parameter, and the BO is linearly coupled with the structural distortion in BaTi$_2$As$_2$O.

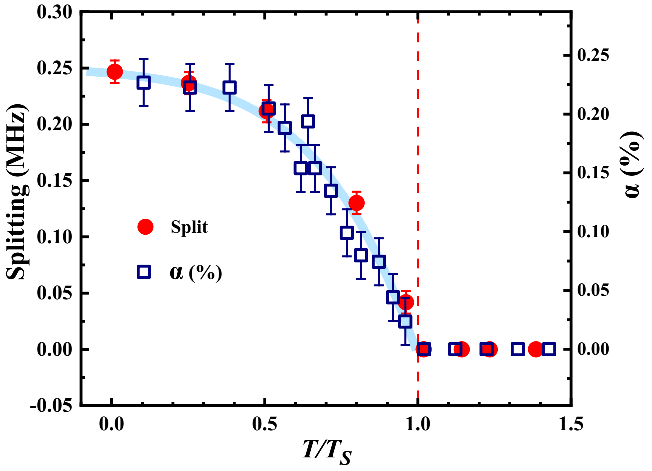

FIG. 7. Scaling of the splitting deduced from Fig. 1(c) with the lattice orthorhombicity α obtained by neutron diffraction [18].

APPENDIX C: SEARCHING THE EVIDENCE FOR POSSIBLE CDW/CHARGE ORDER

To search for the evidence of possible CDW/charge order in BaTi$_2$As$_2$O, we have also tried to measure the satellites of ^{75}As with the external magnetic field H_{ext} along the principal axis of the EFG tensor. As the principal axis of the EFG tensor is along the *c* axis in the high-temperature tetragonal phase, a wide range of frequency was swept (from 80 MHz to 88.3 MHz) with $H_{\text{ext}} \parallel [001]$ at 245.5 K, see the upper panel of Fig. 8. However, only a sharp NMR central transition line of ^{75}As is observed, without any signal of satellites. This is because the satellite is much broader than the central transition line and its signal is completely submerged in the background noise. In contrast to the high-temperature tetragonal phase, both the central transition line and satellite are measured at 2.1 K with H_{ext} along the principal direction $(\theta, \psi) = (49^\circ, 0)$, as shown in the lower panel of Fig. 8. The separating frequency between them is about 5.341 MHz, which is consistent with the $\nu_Q = 5.34$ MHz extracted from the angular-dependent central transition line in Fig. 2(d). In addition, the full width at half maximum (FWHM) of the satellite, $\Delta\nu_Q$, is about 2.86 MHz, which is comparable to the FWHM of $^{121/123}$Sb-NQR spectra in BaTi$_2$Sb$_2$O [19]. From the present NMR satellite spectrum, we do not find any clear evidence

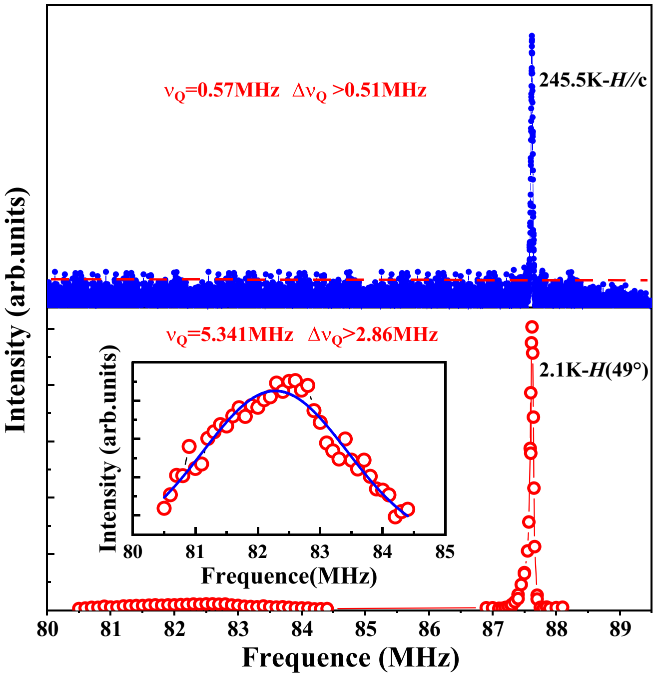

FIG. 8. ^{75}As NMR spectra for BaTi$_2$As$_2$O single crystal measured along the principal axis of the EFG tensor in tetragonal (245.5 K) and orthorhombic (2.1 K) phases, respectively, with the fixed magnetic field of 12 T. The red dashed line stands for an expectation of the satellite peak intensity, which is estimated by considering a similar satellite with the same broadening effect as that at the low temperature. It is clear that the satellite intensity is below the noise level of the background at high temperature.

for commensurate charge order or CDW in $BaTi_2As_2O$. Generally, if there is commensurate charge order or CDW, the satellite would split or broaden. However, we haven't observed any clear splitting for the satellite at 2.1 K, which could exclude any commensurate CDW/charge order with period larger than $2a$. About the possible incommensurate CDW or charge order, since it is not compatible with the well-known structural distortion in this system, it is not considered in our case.

APPENDIX D: POINT CHARGE MODEL CALCULATION ON LATTICE CONTRIBUTION OF EFG TENSOR

As mentioned above, the total EFG tensor (V^{tot}) can be expressed as [34]

$$V^{\mathrm{tot}} = V_{\mathrm{lat}}(1-\gamma_\infty) + V_{\mathrm{val}}, \tag{D1}$$

where V_{lat} is the lattice contribution caused by all the charges outside the ion under consideration and enhanced by antishielding factor $(1-\gamma_\infty)$; V_{val} is the valence contribution, which only exists for subject ions with nonfilled shells. To quantitatively estimate the lattice contribution on the EFG tensor, both the deflection of the principal axis ($d\theta$) and the magnitude of the principal component (V_{ZZ}) are calculated, on the basis of the point-charge model of a $2 \times 2 \times 1$ superlattice. As shown in Fig. 9(a), the possible atomic shift configuration of As and Ti and charge transfer δ between Ti_1 and Ti_2 are indicated by arrows. Since the lattice contribution is dependent on several factors, we took a two-step calculation to simplify our case. We first calculated the δ-dependence of $d\theta$ and V_{ZZ}, see Fig. 9(a), with all the atomic positions fixed. As the value of $d\theta$ is always smaller than 20° (red dots) (only when δ approach to 0.4e, $d\theta$ shows a sudden jump to about 90°), and V_{ZZ} only increases by about 1.4 times from the high-temperature tetragonal phase to low-temperature orthorhombic phase, neither the 49° deflection of the principal axis, nor the one order of magnitude increase of ν_Q (from 0.57 to 5.34 MHz, $\nu_Q = eQV^{\mathrm{tot}}_{ZZ}/h$) can be solely explained as the lattice contribution. Considering the combined effects of lattice distortion and charge transfer, we further calculated the codependence of δ with the atomic shift of Ti and As, respectively, see Figs. 9(c) and 9(d), even though a 49° deflection of the principal axis can never be achieved. Hence, we can conclude that the remarkable changes of the EFG tensor below T_s are mainly attributed to the on-site orbital polarization of ^{75}As itself, which is a direct consequence of the p-d BO between As and Ti. In the whole calculation, except for the atom under consideration, all the rest of the atomic positions are fixed with the crystal structures and the internal atomic positions determined experimentally for tetragonal phase [8], and theoretically for orthorhombic phase [16].

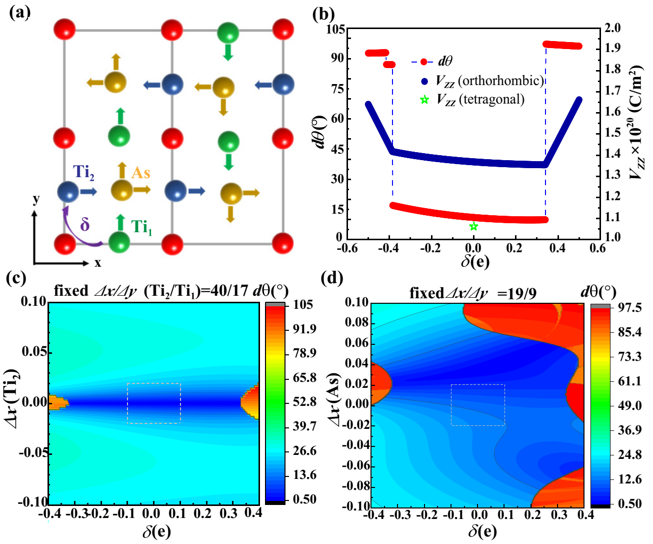

FIG. 9. Calculation results of the lattice contribution on the EFG tensor based on the point charge model of a $2 \times 2 \times 1$ superlattice (a). (b) Both the magnitude of the principal component V_{ZZ} (blue) and the deflection $d\theta$ (red) of the principal axis show a dependence of the charge transfer δ between Ti_1 and Ti_2. As a comparison, the valve of V_{ZZ} in the tetragonal phase is also calculated (green star). (c) and (d) exhibit the codependence of the charge transfer δ with the atomic position shift Δx of Ti and As, respectively, for δ. Here, both the charge transfer δ and the atomic shift are overconsidered, except for the atom under consideration, all the rest of the atomic positions are fixed as given in the theoretical calculation [16], the atomic shift Δx of Ti_2 is given at the ratio of $\frac{\Delta x(Ti_2)}{\Delta y(Ti_1)} = \frac{40}{17}$ in (c), and the atomic shift Δx of As is given at the ratio of $\frac{\Delta x(As)}{\Delta y(As)} = \frac{19}{9}$ in (d). The arrows in (a) show the way of the atomic shift, the color of the maps in (c) and (d) represent the value of $d\theta$, the white dashed frames are guides to the eye to show the relatively reasonable range of the atomic shift and charge transfer.

APPENDIX E: SYMMETRY ANALYSIS ON THE ANISOTROPY OF SPIN-LATTICE RELAXATION

In general, the nuclear spin-lattice relaxation rate divided by temperature $1/T_1T$, which is related to q-averaged low-energy dynamical electron-spin susceptibility, gives information on spin fluctuations. Here, the spin-lattice relaxation rate $1/T_1$ is analyzed as the contribution from the hyperfine field fluctuations perpendicular to the applied field, and is given by

$$\begin{aligned}\left(\frac{1}{T_1}\right)_z &= \frac{(\mu_0\gamma_{\mathrm{n}})^2}{2}\int_{-\infty}^{\infty} dt e^{i\omega t}\left(\left\langle H^{As}_{hf,x}(t), H^{As}_{hf,x}(0)\right\rangle\right.\\ &\quad \left.+ \left\langle H^{As}_{hf,y}(t), H^{As}_{hf,y}(0)\right\rangle\right)\\ &= (\mu_0\gamma_{\mathrm{n}})^2\left(\left|H^{As}_{hf,x}(\omega)\right|^2 + \left|H^{As}_{hf,y}(\omega)\right|^2\right).\end{aligned} \tag{E1}$$

The hyperfine fields H^{As}_{hf} at As sites are determined by the sum of the fields from the four nearest-neighbor Ti electron spins $\mathbf{S}$ in $BaTi_2As_2O$:

$$\boldsymbol{H}^{As}_{hf} = \sum_{i=1}^{4} \boldsymbol{B}_i \cdot \boldsymbol{S}_i = \tilde{A}\boldsymbol{S}, \tag{E2}$$

where $\mathbf{S}_i$ is the electron spin at the ith Ti site, $\mathbf{B}_i$ is the hyperfine coupling tensor between the As nucleus and ith Ti site, and $\tilde{A}$ is the hyperfine coupling tensor ascribed to the four nearest-neighbor Ti electron spins. As the DOS near the Fermi level is almost totally from Ti in $BaTi_2As_2O$, only considering the four nearest-neighbor Ti is sufficient in the discussion. Assuming that the a and b axes are along the nearest-neighbor Ti-Ti direction in the orthorhombic phase, then the hyperfine coupling tensor $\tilde{A}$ can be described as follows:

$$\tilde{A} = \begin{pmatrix} A_a & C & B_1 \\ C & A_b & B_2 \\ B_1 & B_2 & A_c \end{pmatrix}. \tag{E3}$$

A_i is a diagonal term for the i direction ($i = a, b$, and c). B_1 and B_2 are related to the stripe (π, 0) and (0, π) AF correlations and C is related with the checkerboard (π, π) AF correlations. Based on this hyperfine coupling tensor, the fluctuating hyperfine field $H_{hf}^{As}(\omega)$ is obtained with Ti spin fluctuations as shown below, for uncorrelated spin fluctuations:

$$\begin{pmatrix} (1/T_1)_{H\parallel a} \\ (1/T_1)_{H\parallel b} \\ (1/T_1)_{H\parallel c} \end{pmatrix} \propto \begin{pmatrix} |A_b S_b(\omega_{\rm res})|^2 + |A_c S_c(\omega_{\rm res})|^2 \\ |A_c S_c(\omega_{\rm res})|^2 + |A_a S_a(\omega_{\rm res})|^2 \\ |A_a S_a(\omega_{\rm res})|^2 + |A_b S_b(\omega_{\rm res})|^2 \end{pmatrix}, \tag{E4}$$

for stripe (π, 0) correlations:

$$\begin{pmatrix} (1/T_1)_{H\parallel a} \\ (1/T_1)_{H\parallel b} \\ (1/T_1)_{H\parallel c} \end{pmatrix} \propto \begin{pmatrix} |B_1 S_a(\omega_{\rm res})|^2 \\ |B_1 S_a(\omega_{\rm res})|^2 + |B_1 S_c(\omega_{\rm res})|^2 \\ |B_1 S_c(\omega_{\rm res})|^2 \end{pmatrix}, \tag{E5}$$

for stripe (π, π) correlations:

$$\begin{pmatrix} (1/T_1)_{H\parallel a} \\ (1/T_1)_{H\parallel b} \\ (1/T_1)_{H\parallel c} \end{pmatrix} \propto \begin{pmatrix} |C\, S_a(\omega_{\rm res})|^2 \\ |C\, S_b(\omega_{\rm res})|^2 \\ |C\, S_a(\omega_{\rm res})|^2 + |C\, S_b(\omega_{\rm res})|^2 \end{pmatrix}. \tag{E6}$$

According to the definition of the in-plane and out-of-plane anisotropy ratio R_{ac} and R_{ab} in the main text,

$$R_{ac} = \begin{cases} 2 - \dfrac{8}{3+\frac{|A_c S_c(\omega)|^2}{|A_{ab} S_{ab}(\omega)|^2}} & \text{for UC}, \\ \dfrac{2-|\frac{S_c(\omega)}{S_a(\omega)}|^2}{1+1.5\times|\frac{S_c(\omega)}{S_a(\omega)}|^2} & \text{for } (\pi,\ 0), \\ -\frac{1}{3} & \text{for } (\pi,\ \pi), \end{cases} \tag{E7}$$

$$R_{ab} = \begin{cases} \dfrac{2||A_a S_a(\omega)|^2-|A_b S_b(\omega)|^2|}{|A_a S_a(\omega)|^2+|A_b S_b(\omega)|^2+2|A_c S_c(\omega)|^2} & \text{for UC}, \\ \dfrac{2|S_c(\omega)|^2}{2|S_a(\omega)|^2+|S_c(\omega)|^2} = \dfrac{|\frac{S_c(\omega)}{S_a(\omega)}|^2}{2+\frac{S_c(\omega)}{S_a(\omega)}|^2} & \text{for } (\pi,\ 0), \\ 0 & \text{for } (\pi,\ \pi), \end{cases} \tag{E8}$$

where the hyperfine coupling constant $A_{ab} \equiv A_a = A_b$ and the dynamic spin structure factor $|S_a(\omega)| = |S_b(\omega)| = |S_c(\omega|$ in the tetragonal phase. Similar analysis method on $1/(T_1T)$ is also used in iron-based superconductors [23]. As we can see from Figs. 4(c) and 4(d), R_{ab} is of approximately 0.24 and R_{ac} is of approximately 0.45 at 2 K. Hence, the third terms of Eqs. (E7) and (E8) first exclude the possibility of (π, π) AF correlations in BaTi$_2$As$_2$O. Nevertheless, the approximate value 0.45 is very close to the value of R_{ac} deduced from the second term of Eq. (E7), which is exactly equal to 0.4 when $|S_a(\omega)| = |S_c(\omega)|$. This suggests that the abrupt increase of R_{ac} below 140 K [Fig. 4(d)] is due to the emergence of (π, 0) or (0, π) (AF) dynamic spin fluctuations in low temperatures. In fact, as $S_a(\omega)$ cannot be exactly equal to $S_c(\omega)$, nor are the dynamic spin fluctuations at 2 K totally from the stripe AF correlations, the observed value of $R_{ac} \approx 0.45$ at 2 K must be

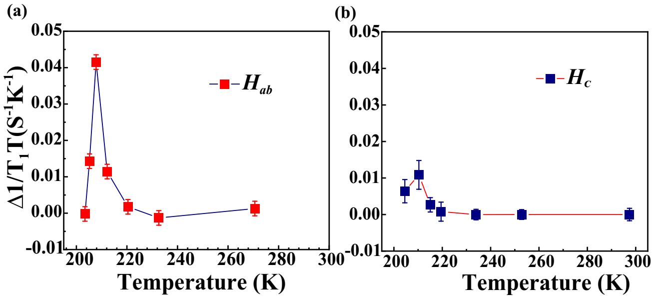

FIG. 10. Correlated critical spin fluctuations around T_S revealed by $1/T_1T$ subtracted the normal part with $H_{\rm ext} \parallel ab$ (a) and $H_{\rm ext} \parallel c$ (b).

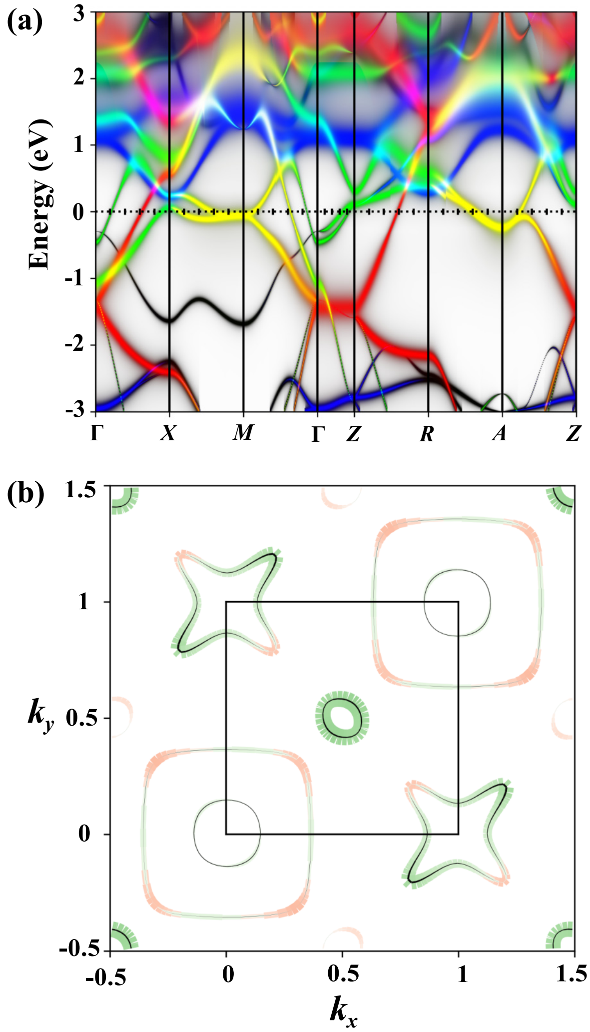

FIG. 11. (a) The electronic band structures of BaTi$_2$As$_2$O calculated using DFT+DMFT with Hubbard $U = 5.0$ eV and Hund's coupling $J = 0.8$ eV at temperature $T = 116$ K. (b) The 2D Fermi surface in the $k_z = 0$ plane in the Brillouin zone of a one-Ti unit cell. The color coding for the band structure and Fermi surface are red: $d_{xz} + d_{yz}$; green: d_{xy}; blue: $d_{yz} - d_{xz}$; black: everything else. Here, z axis is along Ti-O bond and x and y axes are roughly along the Ti-As bonds.

composed of correlated and uncorrelated parts. According to the definition of R_{ac} in the main text,

$$\begin{aligned} R_{ac} &= 2 \times \frac{\frac{1}{2} \times [(T_1T)_a^{-1} + (T_1T)_b^{-1}] - (T_1T)_c^{-1}}{\frac{1}{2} \times [(T_1T)_a^{-1} + (T_1T)_b^{-1}] + (T_1T)_c^{-1}} \times 100\% \\ &= \frac{\frac{1}{2} \times [(\frac{1}{T_1})_a^c + (\frac{1}{T_1})_b^c] + (\frac{1}{T_1})_c^c}{\frac{1}{2} \times [(\frac{1}{T_1})_a + (\frac{1}{T_1})_b] + (\frac{1}{T_1})_c} R_{ac}^c \\ &\quad + \frac{\frac{1}{2} \times [(\frac{1}{T_1})_a^{uc} + (\frac{1}{T_1})_b^{uc}] + (\frac{1}{T_1})_c^{uc}}{\frac{1}{2} \times [(\frac{1}{T_1})_a + (\frac{1}{T_1})_b] + (\frac{1}{T_1})_c} R_{ac}^{uc} \\ &= xR_{ac}^c + (1-x)R_{ac}^{uc}, \end{aligned} \tag{E9}$$

where $(\frac{1}{T_1})_i = (\frac{1}{T_1})_i^c + (\frac{1}{T_1})_i^{uc}$, $(i = a, b, c)$, the superscripts c and uc are corresponding to the correlated and uncorrelated parts, x and $(1-x)$ are the weights of these two parts, respectively. Apart from the data around T_s, the almost constant value of R_{ac} above 140 K suggests $R_{ac}^{uc} \approx 0.15$. By subtracting the normal part of $1/(T_1T)$, the correlated spin fluctuations around T_s are shown in Fig. 10, where $\frac{\Delta 1/T_1T(H_c)}{\Delta 1/T_1T(H_{ab})} \approx \frac{1}{4}$. According to Eq. (E6), the ratio of $\frac{|S_c(\omega)|^2}{|S_a(\omega)|^2}$ caused by the correlated spin fluctuations is of approximately 2/7 at the critical temperature T_s. Assuming that the ratio of $|\frac{S_c(\omega)}{S_a(\omega)}|^2$ is still equal to 2/7 at 2 K for the correlated part, then we have $x \times \frac{2-2/7}{1+1.5\times 2/7} + 0.15(1-x) = 0.45$, based on Eqs. (E7) and Eq. (E9). The solution of this equation is $x = 0.714$ and $(1-x) = 0.286$, suggesting that although the stripe AF correlations emerge at low temperatures, the uncorrelated spin excitation still takes up the main part, which is consistent with the calculated momentum structure of the spin excitations shown in Fig. 5(c). As the in-plane anisotropy R_{ab} from the correlated part is $0.286 \times \frac{2\times 2/7}{2+2/7} = 0.063$, which is much smaller than the value, $0.24 - 0.063 = 0.177$, from the uncorrelated part. This result can also explain why R_{ab}, shown in Fig. 4(c), barely deviates from the temperature dependence of proportional to $\sqrt{T_s - T}$ below 140 K.

APPENDIX F: THEORETICAL INVESTIGATION ON THE ELECTRONIC STRUCTURE AND INSTABILITIES

The electronic structures with orbital resolution for $BaTi_2As_2O$ were calculated using density-functional theory combined with dynamical mean field theory (DFT+DMFT) with Hubbard $U = 5.0$ eV and Hund's coupling $J = 0.8$ eV at temperature $T = 116$ K under $p4/mmm$ symmetry, see Fig. 11(b). The 2D Fermi surface in the $k_z = 0$ plane in the Brillouin zone of a one-Ti unit cell, see Fig. 10(b), shows that the DOS at the Fermi surface are mainly from $d_{xz} + d_{yz}$ and d_{xy} orbits, in which the d_{xy} is actually $3d_{(x^2-z^2)}$ orbital shown in Fig. 3. As the orthorhombic lattice distortion is not considered in the calculation, the Fermi pockets at (0.5, 0.5), (1, 0) and their equivalent positions in Fig. 10(b), which are dominated by d_{xy} and $d_{xz} + d_{yz}$ orbits, break the C_4 rotational symmetry with respect to (0,0) and the center of each pocket, i.e., (0.5, 0.5), (1, 0), etc., suggesting a possibility of electronic nematic instabilities/fluctuation in $BaTi_2As_2O$. This is consistent with our experimental results.

[1] T. Yajima, K. Nakano, F. Takeiri, T. Ono, Y. Hosokoshi, Y. Matsushita, and H. Kageyama, J. Phys. Soc. Jpn. **81**, 103706 (2012).

[2] H.-F. Zhai, W.-H. Jiao, Y.-L. Sun, J.-K. Bao, H. Jiang, X.-J. Yang, Z.-T. Tang, Q. Tao, X.-F. Xu, Y.-K. Li, C. Cao, J.-H. Dai, Z.-A. Xu, and G.-H. Cao, Phys. Rev. B **87**, 100502(R) (2013).

[3] T. Yajima, K. Nakano, F. Takeiri, Y. Nozaki, Y. Kobayashi, and H. Kageyama, J. Phys. Soc. Jpn. **82**, 033705 (2013).

[4] P. Doan, M. Gooch, Z. Tang, B. Lorenz, A. Möller, J. Tapp, and A. M. Guloy, J. Chem. Soc. Am. **134**, 16520 (2012).

[5] F. von Rohr, A. Schilling, R. Nesper, C. Baines, and M. Bendele, Phys. Rev. B **88**, 140501 (2013).

[6] U. Pachmayr and D. Johrendt, Solid State Sci. **28**, 31 (2014).

[7] F. von Rohr, R. Nesper, and A. Schilling, Phys. Rev. B **89**, 094505 (2014).

[8] X. F. Wang, Y. J. Yan, J. J. Ying, Q. J. Li, Zhang, M. Zhang, N. Xu, and X. H. Chen, J. Phys: Condens. Matter **22**, 075702 (2010).

[9] T. C. Ozawa, S. M. Kauzlarich, M. Bieringer, and J. E. Greedan, Chem. Mater. **13**, 1804 (2001).

[10] R. H. Liu, D. Tan, Y. A. Song, Q. J. Li, Y. J. Yan, J. J. Ying, Y. L. Xie, X. F. Wang, and X. H. Chen, Phys. Rev. B **80**, 144516 (2009).

[11] W. E. Pickett, Phys. Rev. B **58**, 4335 (1998).

[12] D. J. Singh, New. J. Phys. **14**, 123003 (2012).

[13] G. Wang, H. Zhang, L. Zhang, and C. Liu, J. App. Phys. **113**, 243904 (2013).

[14] X. W. Yan and Z. Y. Lu, J. Phys: Condens. Matter **25**, 365501 (2013).

[15] D. V. Suetin and A. L. Ivanovskii, J. Alloys Compd. **564**, 117 (2013).

[16] K. Nakano, K. Hongo, and R. Maezono, Sci. Rep. **6**, 29661 (2016).

[17] A. Subedi, Phys. Rev. B **87**, 054506 (2013).

[18] B. A. Frandsen, E. S. Bozin, H. Hu, Y. Zhu, Y. Nozaki, H. Kageyama, and S. J. Billinge, Nat. Commun. **5**, 5761 (2014).

[19] S. Kitagawa, K. Ishida, K. Nakano, T. Yajima, and H. Kageyama, Phys. Rev. B **87**, 060510 (2013).

[20] Y. Nozaki, K. Nakano, T. Yajima, H. Kageyama, B. Frandsen, L. Liu, S. Cheung,T. Goko, Y. J. Uemura, T. S. J. Munsie, T. Medina, G. M. Luke, J. Munevar, D. Nishio-Hamane, and C. M. Brown, Phys. Rev. B **88**, 214506 (2013).

[21] N. R. Davies, R. D. Johnson, A. J. Princep, L. A. Gannon, J.-Z. Ma, T. Qian, P. Richard, H. Li, M. Shi, H. Nowell, P. J. Baker, Y. G. Shi, H. Ding, J. Luo, Y. F. Guo, and A. T. Boothroyd, Phys. Rev. B **94**, 104515 (2016).

[22] Q. Song, Y. J. Yan, Z. R. Ye, M. Q. Ren, D. F. Xu, S. Y. Tan, X. H. Niu, B. P. Xie, T. Zhang, R. Peng, H. C. Xu, J. Jiang, and D. L. Feng, Phys. Rev. B **93**, 024508 (2016).

[23] S. Kitagawa, Y. Nakai, T. Iye, K. Ishida, Y. Kamihara, M. Hirano, and H. Hosono, Phys. Rev. B **81**, 212502 (2010).

[24] H. C. Xu, M. Xu, R. Peng, Y. Zhang, Q. Q. Ge, F. Qin, M. Xia, J. J. Ying, X. H. Chen, X. L. Yu, L. J. Zou, M. Arita, K.

Shimada, M. Taniguchi, D. H. Lu, B. P. Xie, and D. L. Feng, Phys. Rev. B **89**, 155108 (2014).

[25] S. Y. Tan, J. Jiang, Z. R. Ye, X. H. Niu, Y. Song, C. L. Zhang, and D. L. Feng, Sci. Rep. **5**, 9515 (2015).

[26] H. Nakaoka, Y. Yamakawa, and H. Kontani, Phys. Rev. B **93**, 245122 (2016).

[27] G. Zhang, J. K. Glasbrenner, R. Flint, I. I. Mazin, and R. M. Fernandes, Phys. Rev. B **95**, 174402 (2017).

[28] R. Fernandes, A. Chubukov, and J. Schmalian, Nat. Phys. **10**, 97 (2014).

[29] S. H. Baek, D. V. Efremov, J. M. Ok, J. S. Kim, and B. Büchner, Nat. Mater. **14**, 210 (2015).

[30] A. E. Bühmer, T. Arai, F. Hardy, T. Hattori, T. Iye, T. Wolf, and C. Meingast, Phys. Rev. Lett. **114**, 027001 (2015).

[31] G. M. Volkoff, Can. J. Phys. **31**, 820 (1953).

[32] K. Takubo, R. Comin, D. Ootsuki, T. Mizokawa, H. Wadati, Y. Takahashi, and S. Pyon, Phys. Rev. B **90**, 081104 (2014).

[33] M. Fu, D. A. Torchetti, T. Imai, F. L. Ning, J. Q. Yan, and A. S. Sefat, Phys. Rev. Lett. **109**, 247001 (2012).

[34] K. D. Sen and P. T. Narasimhan, Phys. Rev. A **16**, 1786 (1977).

[35] X. Ren, Z. D. Ji, G. Q. Wang, D. W. Song, T. Wu, X. H. Chen, and Y. Li, unpublished (Raman scattering experiment from Prof. Y. Li group in Peking university), and private communication with Prof. Y. Liu in Zhejiang University (resonant x-ray scattering).

[36] J. A. Wilson, F. J. Di Salvo, and S. Mahajan, Adv. Phys. **24**, 117 (1975).

[37] D. W. Shen, B. P. Xie, J. F. Zhao, L. X. Yang, L. Fang, J. Shi, R. H. He, D. H. Lu, H. H. Wen, and D. L. Feng, Phys. Rev. Lett. **99**, 216404 (2007).

[38] D. W. Shen, Y. Zhang, L. X. Yang, J. Wei, H. W. Ou, J. K. Dong, B. P. Xie, C. He, J. F. Zhao, B. Zhou, M. Arita, K. Shimada, H. Namatame, M. Taniguchi, J. Shi, and D. L. Feng, Phys. Rev. Lett. **101**, 226406 (2008).

[39] M. D. Johannes and I. I. Mazin, Phys. Rev. B **77**, 165135 (2008).

[40] G. Kotliar, S. Y. Savrasov, K. Haule, V. S. Oudovenko, O. Parcollet, and C. A. Marianetti, Rev. Mod. Phys. **78**, 865 (2006).

[41] P. Blaha, K. Schwarz, G. Madsen, D. Kvasnicka, and J. Luitz, WIEN2k, An Augmented Plane Wave + Local Orbitals Program for Calculating Crystal Properties. Technische Universität Wien (2001).

[42] K. Haule, C. H. Yee, and K. Kim, Phys. Rev. B **81**, 195107 (2010).

[43] K. Haule, Phys. Rev. B **75**, 155113 (2007).

[44] P. Werner, A. Comanac, L. de Medici, M. Troyer, and A. J. Millis, Phys. Rev. Lett. **97**, 076405 (2006).

[45] Z. P. Yin, K. Haule, and G. Kotliar, Nat. Phys. **10**, 845 (2014).

[46] P. Giannozzi, S. Baroni, N. Bonini, M. Calandra, R. Car, C. Cavazzoni, and A. Dal Corso, J. Phys.: Condens. Matter **21**, 395502 (2009).

[47] P. Giannozzi, O. Andreussi, T. Brumme, O. Bunau, M. B. Nardelli, M. Calandra, and N. Colonna, J. Phys.: Condens. Matter **29**, 465901 (2017).

[48] J. P. Perdew, K. Burke, and M. Ernzerhof, Phys. Rev. Lett. **77**, 3865 (1996).

[49] See Supplemental Material at http://link.aps.org/supplemental/10.1103/PhysRevB.98.235142 for information on the general physical properties of our sample, the NMR analysis, the fitting procedure and simulation of the angular dependent NMR central frequency, the anisotropy of magnetic Knight shift in the BO phase, and the simulation of ^{75}As NMR central spectra based on NQI effect.

[50] X.-L. Yu, D.-Y. Liu, Y.-M. Quan, J. Wu, H.-Q. Lin, K. Chang, and L.-J. Zou, Phys. Rev. B **96**, 125138 (2017).

[51] T. Ritschel, J. Trinckauf, K. Koepernik, B. Büchner, M. v. Zimmermann, H. Berger, Y. I. Joe, P. Abbamonte, and J. Geck, Nat. Phys. **11**, 328 (2015).